Simple synthesis of hollow Pt–Pd nanospheres supported on reduced graphene oxide for enhanced methanol electrooxidation

CrossMark

Shan-Shan Li [a,b], Jianyan Yu [c], Yuan-Yuan Hu [a,b], Ai-Jun Wang [a,b,*], Jian-Rong Chen [a,b], Jiu-Ju Feng [a,b,*]

[a] College of Chemistry and Life Science, Zhejiang Normal University, Jinhua 321004, China
[b] College of Geography and Environmental Science, Zhejiang Normal University, Jinhua 321004, China
[c] Key Laboratory of the Ministry of Education for Advanced Catalysis Materials, Institute of Physical Chemistry, Zhejiang Normal University, 321004 Jinhua, China

HIGHLIGHTS

- A rapid and simple method was developed for large-scale preparation of Pt–Pd hollow nanospheres supported on RGO nanosheets.
- No surfactant, seed, or template was involved during the mild synthetic process.
- The as-prepared nanocomposites displayed the enhanced electrocatalytic activity and stability for methanol oxidation.

GRAPHICAL ABSTRACT
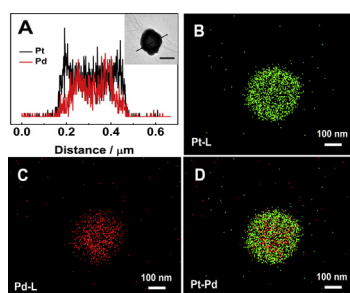
ARTICLE INFO

ABSTRACT

Shape-controlled synthesis of bimetallic catalysts attracts increasing attention, because their catalytic performance is closely correlated with the size, shape and crystal structure. In this report, a rapid and simple route is developed for large-scale synthesis of Pt–Pd hollow nanospheres (Pt–Pd HNSs) supported on reduced graphene oxide nanosheets (RGOs) under mild conditions, while no surfactant, seed, or template is involved. The as-prepared nanocomposites display the improved electrocatalytic activity and better stability for methanol oxidation in alkaline media, compared with commercial Pt black and Pd black catalysts. This work may open a new route for construction of Pt-based bimetallic catalysts in fuel cells.

© 2014 Elsevier B.V. All rights reserved.

1. Introduction

Fuel cells are promising green energy sources for future energy conversion devices [1]. Among them, significant attention is focused on direct methanol fuel cells (DMFC), owing to their practical energy density, compact design and easy refueling [2,3]. For their potential commercialization, there are still several obstacles unsolved such as slow reaction kinetics, methanol crossover and large electrode overpotential [4,5]. For improving their utilization efficiency, a variety of hierarchical nanostructures have been synthesized with specific morphology, including spheres [6,7], wires [8,9], flowers [10], cubes [11], and plates [12]. Among them, hollow nanostructures provide the enhanced catalytic performance

---

* Corresponding authors. College of Chemistry and Life Science, Zhejiang Normal University, Jinhua 321004, China. Tel./fax: +86 579 82282269.
E-mail addresses: ajwang@zjnu.cn (A.-J. Wang), jjfeng@zjnu.cn, jjfengnju@gmail.com (J.-J. Feng).

and utilization efficiency because of their lower density and higher surface area, unlike their solid counterparts [13].

Furthermore, bimetallic catalysts have synergistic effects on the improved catalytic activity and strong poisoning resistance [14–16]. Particularly, Pt–Pd alloy nanostructures are significant for their enhanced catalytic performance as catalysts [15,17]. For example, Wang et al. [18] synthesized the Pt–Pd bimetallic nanodendrites with a good catalytic activity. To date, many methods have been developed such as wet-chemical synthesis [6,18], electrochemical deposition [19], thermal treatment [20], and self-assembly [21].

Graphene provides a large electrode surface area and high electric conductivity for its two-dimensional structures [22,23], and is usually used as an attractive support for loading metal nanoparticles with the following aspects of advantages [24,25]. Firstly, graphene can fix and well disperse a catalyst, which are beneficial to keep the catalyst with original shape, size, and surface state [26]. Secondly, the graphene supporting catalyst exhibits a significant decrease in Brownian motions, causing poor colloidal stability and thereby easy recycling from the reaction media, compared with the isolated catalyst [26].

Recently, graphene-based metal nanostructures offer a new class of catalysts, which show improved catalytic performance in fuel cells [27]. For methanol oxidation, Li and co-workers [6] prepared porous Pt–Pd nanospheres anchored on reduced graphene oxide nanosheets (RGOs). Meanwhile, Lu et al. [28] synthesized PtPd nanocubes deposited on graphene with the improved activity and durability.

Herein, we develop a rapid and facile approach to prepare Pt–Pd hollow nanospheres (Pt–Pd HNSs) supported on RGOs via a one-pot synthetic strategy without any surfactant, seed, or template. The as-prepared nanocomposites display the improved electrochemical performance for methanol oxidation in alkaline media, and thereby can be used as a promising catalyst in fuel cells.

2. Experimental

2.1. Chemicals

Graphite powder (99.95%, 8000 mesh), chloroplatinic acid (H_2PtCl_6), palladium chloride ($PdCl_2$), Pt black and Pd black catalysts were purchased from Shanghai Aladdin Chemistry Co. Ltd (China). All other chemicals were of analytical grade and used as received.

2.2. Preparation of the RGOs/Pt–Pd HNSs

Graphene oxide (GOs) was prepared from natural graphite powder via acid-oxidation based on the modified Hummers' method [6,29]. After removal of residual salts and acids, the resultant dispersion was ultrasonicated to obtain exfoliated GOs.

For synthesis of the RGOs/Pt–Pd HNSs, the aqueous solution of the GOs suspension was ultrasonicated for at least 30 min. Then, 5.0 mL of the GOs suspension (0.5 mg mL^{-1}), 1.5 mL of H_2PtCl_6 (10 mM), 1.5 mL of $PdCl_2$ (10 mM), and 0.5 mL of NaOH (0.1 M) solutions were mixed together under stirring. After homogeneous mixing, 0.5 mL of freshly prepared ascorbic acid (AA, 0.1 M) solution was slowly added to the mixed solution under stirring. The mixture was heated in a water-bath at 60 °C for 30 min without any agitation. The final products were collected by centrifugation, thoroughly washed with water and ethanol, and dried in vacuum for further characterization. For comparison, RGOs/Pt and RGOs/Pd nanocomposites were prepared in a similar way, only using H_2PtCl_6 or $PdCl_2$ as precursors, while other conditions were kept unchanged.

2.3. Characterization

The morphology and structure of the products were characterized by transmission electron microscope (TEM) and high resolution TEM (HR-TEM) on a JEM-2100F transmission electron microscope operating at an accelerating voltage of 200 kV. The elemental mappings were recorded on the scanning transmission electron microscope with a high-angle annular dark-field (HAADF-STEM) detector operating at 30 kV (HITACHI S-5500). The chemical composition was examined by using energy dispersive spectroscopy (EDS) with Vantage Digital Acquisition Engine (Thermo Noran, USA). The crystal structures were determined by X-ray diffraction (XRD, Rigaku Dmax-2000 diffractometer) with Cu Kα radiation. Fourier transform infrared (FT-IR) spectra were recorded on a Nicolet NEXUS670 Fourier transform infrared spectrometer. X-ray photoelectron spectra were acquired by using a Thermo Scientific Escalab 250 K-Alpha XPS spectrometer with Al Kα X-ray radiation (1486.8 eV). Raman spectra were recorded on a Renishaw Raman system model 1000 spectrometer, with a He/Ne laser (633 nm). Thermogravimetric analysis (TGA) was performed on a simultaneous thermo-gravimetric analyzer (NETZSCH STA 449C). The samples were heated under air atmosphere from room temperature to 800 °C at a rate of 10 °C min^{-1}.

2.4. Electrochemical measurements

The electrochemical measurements were conducted with a conventional three-electrode cell on a CHI 660D electrochemical workstation (CH Instruments, Chenhua Co., Shanghai, China), in which a bare or modified glassy carbon electrode (GCE, 3 mm in diameter) was used as working electrode, a Pt foil as counter electrode, and a saturated calomel electrode (SCE) as reference electrode, respectively.

For preparation of the RGOs/Pt–Pd HNSs modified electrodes, 2 mg of the RGOs/Pt–Pd HNSs was placed into 1.0 mL of water and dispersed by ultrasonication for 30 min to obtain a homogeneous suspension (2 mg mL^{-1}). Next, 6 μL of the suspension was casted onto the electrode surface with a microsyringe and dried at room temperature. Similarly, the RGOs/Pt, RGOs/Pd, Pt black and Pd black catalysts modified electrodes were fabricated under the same conditions. The specific load of each catalyst was 0.17 mg cm^{-2} on the electrode surface.

To investigate the electrocatalytic activity and stability of the RGOs/Pt–Pd HNSs modified electrode, electrochemical experiments were performed in 1.0 M NaOH containing 1.0 M methanol at a scan rate of 50 mV s^{-1}.

3. Results and discussion

TEM and HR-TEM experiments confirm the formation of the RGOs/Pt–Pd HNSs (Figs. 1A and 2A). The Pt–Pd HNSs are clearly anchored on the RGOs with an average diameter of 170 ± 1 nm, based on the associated size distribution histogram (inset in Fig. 1A). Meanwhile, the HAADF-STEM image verifies the formation of the shell-like structures, exhibiting an internal cavity with the shell thickness of ca. 50 nm (inset in Fig. 1B). HAADF-STEM-EDS measurements were performed to get more information about the elemental distribution in the Pt–Pd HNSs. As shown in Fig. 1B, the cross-sectional compositional line profiles reveal hollow structures [30] and a homogeneous distribution of Pt and Pd in a single nanosphere, which is consistent with the XPS measurements (Fig. 3). The EDS elemental mapping images confirm uniform distribution of Pt and Pd again (Fig. 1C–E). In addition, HR-TEM image (Fig. 2B) shows clear lattice fringes with the lattice spacing distance of 0.230 nm, corresponding to the (111) planes of face-centered
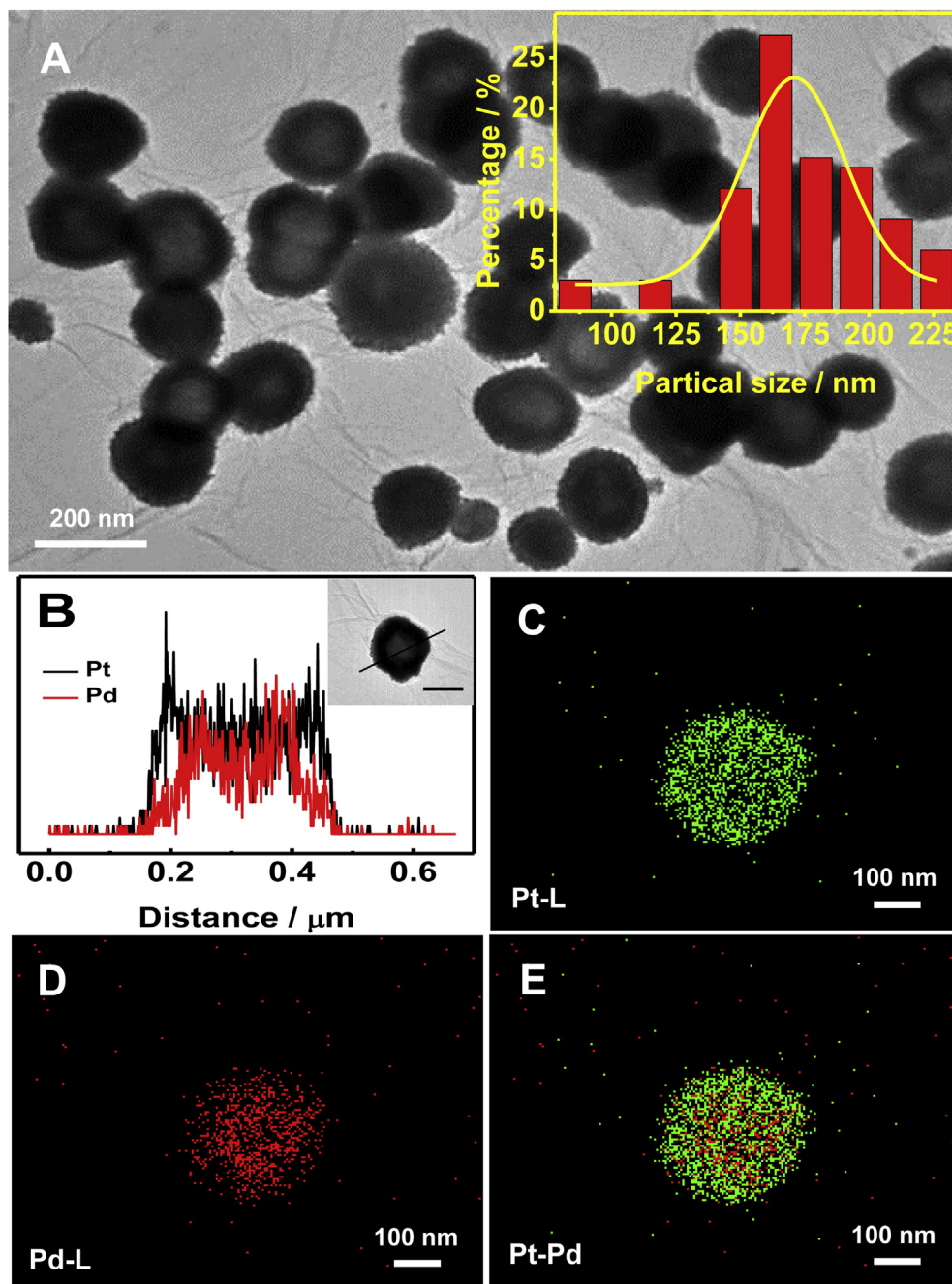
Fig. 1. TEM images of the RGOs/Pt–Pd HNSs (A) and the corresponding particle size distribution histogram (inset in Fig. 1A). Cross-sectional compositional line profiles of a Pt–Pd HNSs (B) and the HAADF-STEM image of a Pt–Pd HNSs (inset in Fig. 1B, scale bar indicates 100 nm). HAADF-STEM-EDS mapping images of the Pt (C), Pd (D), and Pt–Pd (E) elements, respectively.

cubic (fcc) Pt–Pd alloy [31]. Meanwhile, their good crystallinity is demonstrated by the selected area electronic diffraction (SAED) pattern (inset in Fig. 2B).

A possible formation mechanism of inside-out Ostwald ripening is proposed to describe the template-free formation of the Pt–Pd HNSs [32]. At the initial stage, amorphous solid nanospheres are formed by reducing the precursors. With the extension of time, the outer layer of the nanospheres first crystallizes for its direct contact with surrounding reaction media. As a result, its inner part has a strong tendency to dissolve, which provides the driving force for spontaneous inside-out Ostwald ripening. The dissolution process could initiate at regions either near the outer part or the inner core

to produce hollow spheres, presumably depending on the packing of primary particles and ripening characteristics.

As displayed in Fig. 2C, EDS spectrum verifies the coexistence of Pt and Pd in the Pt–Pd nanospheres, where the molar ratio of Pt to Pd is ca. 1:1. Besides, the elements of C, O, and Cu are also detected. Specifically, the peak of C comes from the RGOs and supporting film of the copper mesh, while the existence of oxygen signal is due to incomplete reduction of the GOs [33]. Additionally, the signals of Cu are attributed to the copper mesh used for the TEM tests.

XRD measurements confirm good crystallinity of the RGOs/Pt–Pd HNSs (Fig. 2D, curve a), as supported by the SAED pattern. The representative diffraction peaks at 40.2°, 46.7°, 68.2°, 82.1°, and
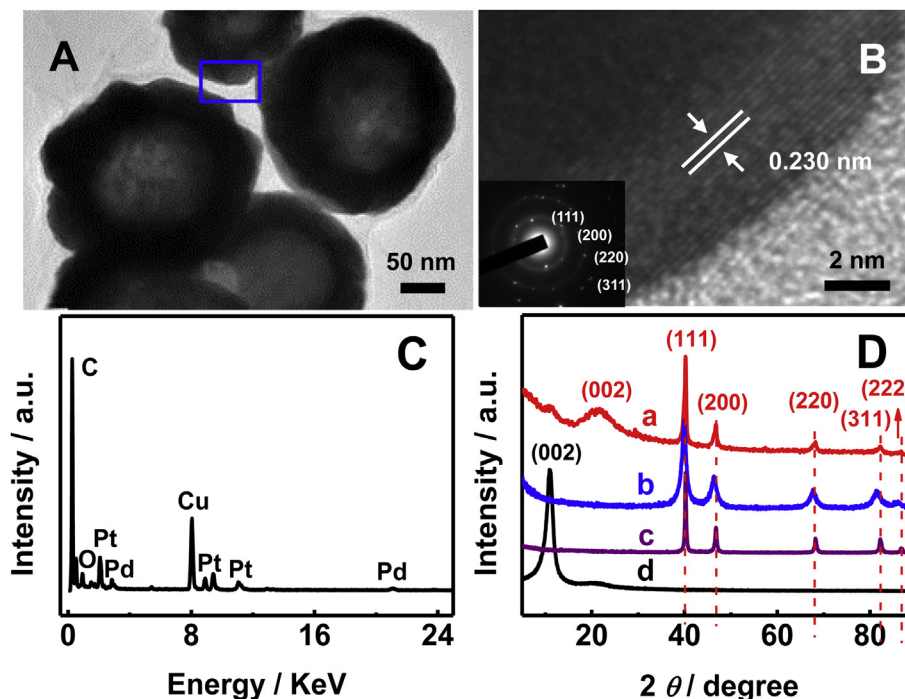
Fig. 2. HR-TEM (A, B) images of the RGOs/Pt−Pd HNSs and the SAED patterns marked in different positions. EDS pattern of the RGOs/Pt−Pd HNSs (C). XRD patterns (D) of the RGOs/Pt−Pd HNSs (curve a), Pt black (curve b), Pd black (curve c), and pure GOs (curve d) samples, respectively.

86.7° are assigned to the (111), (200), (220), (311), and (222) planes of Pt−Pd alloy [34,35], respectively, which are located between commercial Pt black (Fig. 2D, curve b) and Pd black (Fig. 2D, curve c) catalysts, confirming the alloy formation between Pt and Pd. Notably, the relative intensity of the (111) to (200) planes is slightly

larger for the RGOs/Pt−Pd HNSs (1.94), compared with Pt black (1.75) and Pd black (1.83) catalysts, suggesting that the Pt−Pd HNSs are dominated by the (111) planes. These results agree well with the HR-TEM and SAED analysis, indicating that these structures might have special crystallographic orientation. Meanwhile, a broad
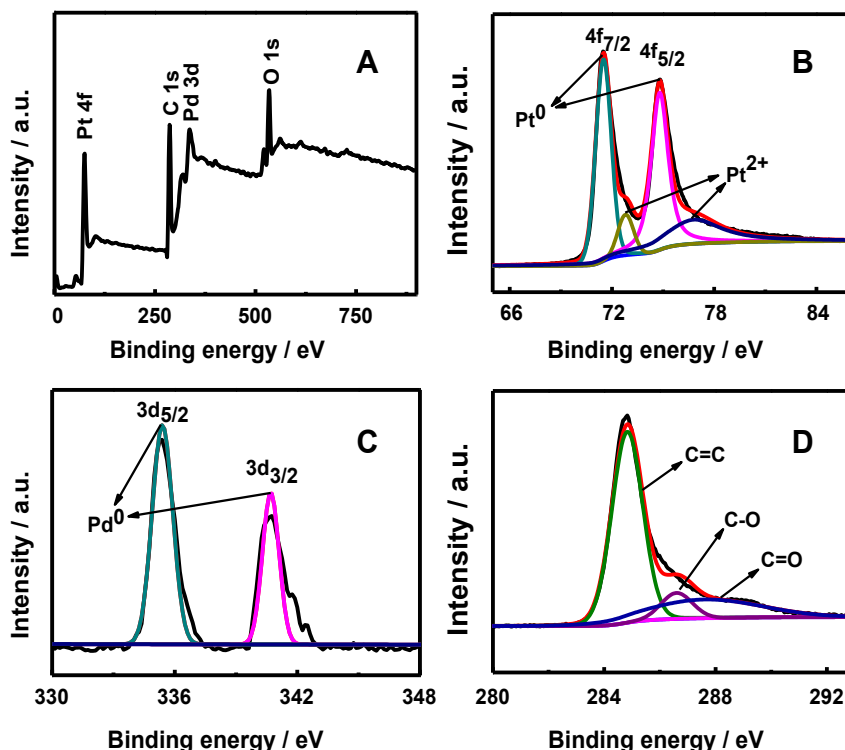

Fig. 3. XPS survey (A), and high resolution Pt 4f (B), Pd 3d (C), and C 1s (D) spectra of the RGOs/Pt−Pd HNSs.
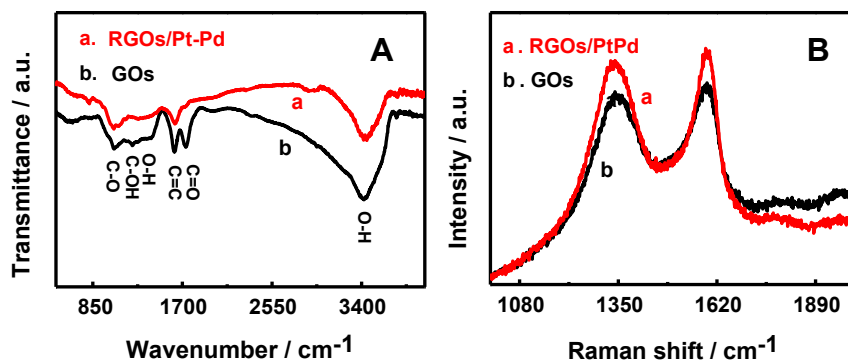
Fig. 4. FT-IR (A) and Raman (B) spectra of the RGOs/Pt–Pd HNSs (curve a) and pure GOs (curve b) samples, respectively.

diffraction peak at 23° is detected, different from the GOs sample with a strong peak at 11° corresponding to the (002) planes of the GOs (Fig. 2D, curve d).

XPS analysis was employed to investigate the surface chemistry modifications of the RGOs/Pt–Pd HNSs. As illustrated in Fig. 3A, the main XPS peaks at 74, 288, 336, and 533 eV are assigned to Pt 4f, C 1s, Pd 3d, and O 1s in the survey spectrum, respectively. The elemental amounts of C, O, Pt, and Pd are 60.85, 16.42, 12.08, and 10.65, respectively. Furthermore, the molar ratio of Pt to Pd is about 1:1, which is in accordance with the EDS results (Fig. 2C).

As showed in Fig. 3B, Pt 4f can be deconvoluted into two pairs of peaks, i.e., 71.5 eV (Pt $4f_{7/2}$), 74.8 eV (Pt $4f_{5/2}$), 72.8 eV (Pt $4f_{7/2}$), and 76.8 eV (Pt $4f_{5/2}$), which are assigned to metallic Pt and Pt^{2+} [36,37], respectively. However, the Pd 3d peak can be deconvoluted into only one pair of peaks (Fig. 3C), i.e., 335.4 eV (Pd $3d_{5/2}$), and 340.8 eV (Pd $3d_{3/2}$), which are assigned to metallic Pd [36,37]. By measuring their relative peak intensities, it is found that the metallic Pt and Pd are the predominant species, which are associated with the enhanced methanol oxidation and electrochemical activity [37]. Besides, the peak at 284.8 eV is attributed to the binding energy of C 1s, which can be further separated into three peaks at 284.8, 286.6, and 287.6 eV (Fig. 3D), corresponding to the C=C, C–O, and C=O groups [38,39]. The peaks related to the oxygen functionalities are much weaker in the present system, compared with the C=C peak, indicating efficient reduction of the GOs. The XPS analysis confirms effective assembly of the Pt–Pd HNSs on the surface of the RGOs.

Furthermore, FT-IR and Raman spectra are two powerful tools to characterize graphene-based catalysts. For the RGOs/Pt–Pd HNSs (Fig. 4A, curve a), there are two weak peaks and a strong broad one

observed at 1627, 1060, and 3417 cm^{-1} in the FT-IR spectra, which are attributed to the skeletal vibration of C=C, stretching vibration of C–O [40], and O–H stretching vibration of C–OH and water [41], respectively. These observations are different from the GOs (Fig. 4A, curve b), where the peaks related to the oxygen functionalities are much stronger in comparison with the C=C peak. It indicates complete removal of oxygen-containing functional groups from the RGO surfaces.

Similarly, the Raman spectrum of the RGOs/Pt–Pd HNSs displays two strong peaks at 1340 and 1594 cm^{-1} (Fig. 4B, curve a), corresponding to the D and G bands, respectively. Meanwhile, the G band is broadened and red shifted, unlike those from the GOs (Fig. 4B, curve b) and graphite samples [42]. Moreover, the intensity ratio (denoted as I_D/I_G, Table S1, Supporting information) is slightly increased for the RGOs/Pt–Pd HNSs, suggesting well preservation of the graphene with highly crystalline structures even after chemical deposition of the Pt–Pd nanocatalysts [31,43]. This is important to achieve good electrical conductivity in the nanocomposites.

TGA analysis was performed to check the weight loss of the RGOs/Pt–Pd HNSs (Fig. S1, curve a, Supporting information). The weight loss below 200 °C is attributed to the loss of water absorbed on the graphene nanosheets and the removal of some oxygenated functional groups. Impressively, the weight loss is much lower in the temperature range of 200–600 °C, compared with the GOs under the same conditions (Fig. S1, curve b, Supporting information). It means the decrease of oxygenated functional groups on the graphene [37,44]. Additionally, the load of the Pt–Pd HNSs is about 90 wt%.

The CO-stripping voltammogram was recorded to evaluate the electrochemically active surface area (EASA) of a catalyst, assuming a value of 210 $\mu C\ cm^{-2}$ for the oxidation of a CO monolayer [6,28,37,45]
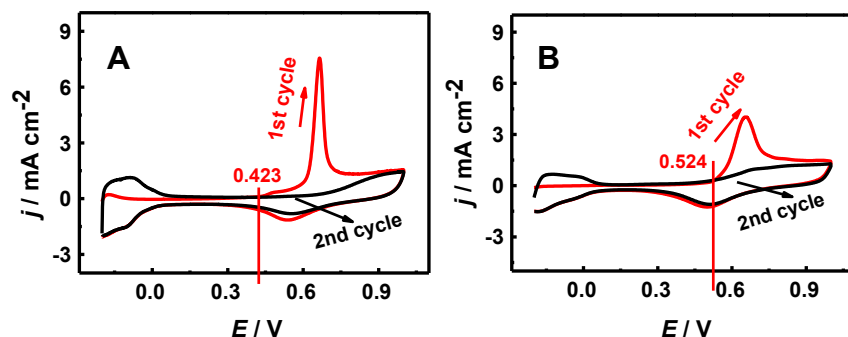

Fig. 5. CO-stripping voltammograms of the RGOs/Pt–Pd HNSs (A) and Pt black (B) catalysts modified electrodes in 0.5 M H_2SO_4 at a scan rate of 50 mV s^{-1}.
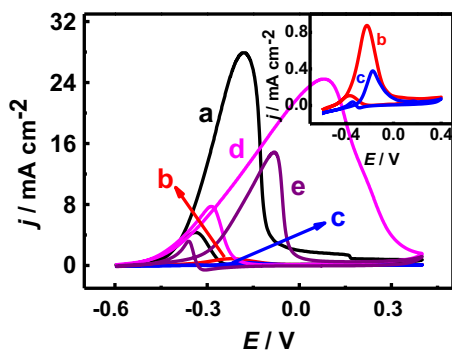
Fig. 6. Cyclic voltammograms of the RGOs/Pt–Pd HNSs (curve a), RGOs/Pt (curve b), RGOs/Pd (curve c), Pt black (curve d) and Pd black (curve e) catalysts modified electrodes in the presence of 1.0 M methanol in 1.0 M NaOH.

$$\mathrm{EASA}\left(\mathrm{m^2\ g^{-1}}\right) = Q/(m \times 210)$$

where Q is the charge of CO desorption electrooxidation in microcoulomb (μC) and m represents the load of metal (g). The EASA of the RGOs/Pt–Pd HNSs (Fig. 5A) is about 18.5 m^2 g^{-1}, which is much larger than that of Pt black catalyst (16.6 m^2 g^{-1}) (Fig. 5B). Besides, the onset potential of the RGOs/Pt–Pd HNSs (0.423 V) shifts negatively, compared with that of the Pt black catalyst (0.524 V).

Fuel cells operating in alkaline conditions have several important advantages, such as the improved reaction kinetics, less corrosive environment to the electrodes, and high transfer rate of species to the anode [21,46–48]. So, the cyclic voltammograms (CVs) of the RGOs/Pt–Pd HNSs were recorded in 1.0 M NaOH containing 1.0 M methanol (Fig. 6, curve a). The onset potential and forward peak potential negatively shift. The forward peak current density (j_F) is ca. 28 mA cm^{-2}, which is much higher than those of the RGOs/Pt (0.88 mA cm^{-2}, Fig. 6, curve b), RGOs/Pd (0.38 mA cm^{-2}, Fig. 6, curve c), Pt black (24 mA cm^{-2}, Fig. 6, curve d) and Pd black (15 mA cm^{-2}, Fig. 6, curve e) catalysts under the same conditions. These results indicate the enhanced electrocatalytic activity of the RGOs/Pt–Pd HNSs, owing to the special structures of the RGOs/Pt–Pd HNSs with more active sites available.

The stability of the RGOs/Pt–Pd HNSs was investigated by chronoamperometry at an applied potential of −0.3 V in the electrolyte of 1.0 M methanol + 1.0 M NaOH (Fig. 7, curve a), in which the polarization current slowly decreases at the initial stage. The anodic current density is higher than those of the RGOs/Pt (Fig. 7, curve b), RGOs/Pd (Fig. 7, curve c), Pt black (Fig. 7, curve d), and Pd black (Fig. 7, curve e) catalysts modified electrodes. These results
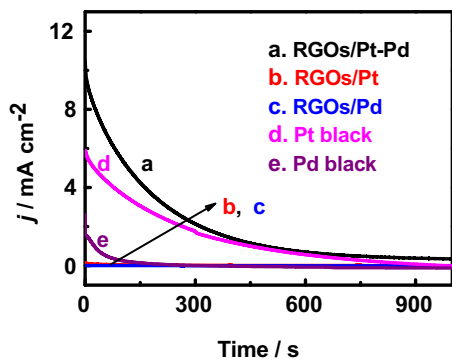

Fig. 7. Chronoamperometric curves of the RGOs/Pt–Pd HNSs (curve a), RGOs/Pt (curve b), RGOs/Pd (curve c), Pt black (curve d) and Pd black (curve e) catalysts modified electrodes in the presence of 1.0 M methanol in 1.0 M NaOH at −0.3 V.
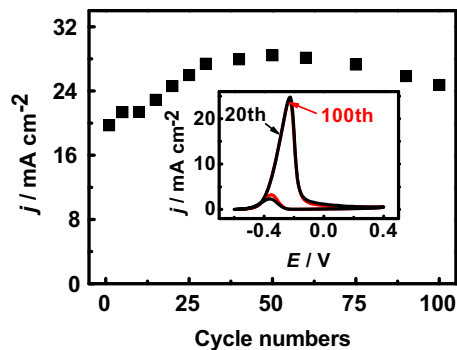

Fig. 8. Forward peak current density (j_F) as a function of the potential scanning cycles of the RGOs/Pt–Pd HNSs modified electrode in the presence of 1.0 M methanol in 1.0 M NaOH. Inset shows the corresponding 20th and 100th cyclic voltammograms.

demonstrate the improved electrocatalytic activity and superior stability of the RGOs/Pt–Pd HNSs. Employing the j_F of the 20th cycle on the RGOs/Pt–Pd NSs as the reference, the j_F remains at 99% after 100 cycles (Fig. 8), further revealing better stability of the RGOs/Pt–Pd HNSs.

4. Conclusions

A simple and rapid one-pot method was developed for large-scale fabrication of the RGOs/Pt–Pd HNSs under mild conditions, without using any seed, surfactant, or template. The electrochemical measurements demonstrated that the RGOs/Pt–Pd HNSs had the enhanced catalytic activity and better stability toward methanol oxidation because of the enlarged surface area and improved electrical conductivity. The as-developed method opens a new way for design and construction of other catalysts in fuel cells.

Acknowledgment

Appendix A. Supplementary data

Supplementary data related to this article can be found at http://dx.doi.org/10.1016/j.jpowsour.2013.12.098.

References

[1] L. Carrette, K.A. Friedrich, U. Stimming, ChemPhysChem 1 (2000) 162–193.
[2] J. Li, Y. Liang, Q. Liao, X. Zhu, X. Tian, Electrochim. Acta 54 (2009) 1277–1285.
[3] H. Liu, C. Song, L. Zhang, J. Zhang, H. Wang, D.P. Wilkinson, J. Power Sources 155 (2006) 95–110.
[4] T. Iwasita, Electrochim. Acta 47 (2002) 3663–3674.
[5] K. Ding, H. Jia, S. Wei, Z. Guo, Ind. Eng. Chem. Res. 50 (2011) 7077–7082.
[6] S.-S. Li, J.-J. Lv, Y.-Y. Hu, J.-N. Zheng, J.-R. Chen, A.-J. Wang, J.-J. Feng, J. Power Sources 247 (2014) 213–218.
[7] Z. Liu, B. Zhao, C. Guo, Y. Sun, Y. Shi, H. Yang, Z. Li, J. Colloid Interface Sci. 351 (2010) 233–238.
[8] M. Hasan, S.B. Newcomb, J.F. Rohan, K.M. Razeeb, J. Power Sources 218 (2012) 148–156.
[9] H. Wang, C. Xu, F. Cheng, M. Zhang, S. Wang, S.P. Jiang, Electrochem. Commun. 10 (2008) 1575–1578.
[10] B. Fang, C. Zhang, W. Zhang, G. Wang, Electrochim. Acta 55 (2009) 178–182.
[11] Q. Wang, B. Geng, B. Tao, J. Power Sources 196 (2011) 191–195.
[12] H. Huang, H. Chen, D. Sun, X. Wang, J. Power Sources 204 (2012) 46–52.
[13] H.-P. Liang, H.-M. Zhang, J.-S. Hu, Y.-G. Guo, L.-J. Wan, C.-L. Bai, Angew. Chem. Int. Ed. 43 (2004) 1540–1543.

[14] Y. Hu, H. Zhang, P. Wu, H. Zhang, B. Zhou, C. Cai, PCCP 13 (2011) 4083−4094.
[15] S. Guo, S. Dong, E. Wang, ACS Nano 4 (2009) 547−555.
[16] L. Feng, G. Gao, P. Huang, X. Wang, C. Zhang, J. Zhang, S. Guo, D. Cui, Nanoscale Res. Lett. 6 (2011) 1−10.
[17] Y. Liu, M. Chi, V. Mazumder, K.L. More, S. Soled, J.D. Henao, S. Sun, Chem. Mater. 23 (2011) 4199−4203.
[18] L. Wang, Y. Nemoto, Y. Yamauchi, J. Am. Chem. Soc. 133 (2011) 9674−9677.
[19] R. Ojani, J.B. Raoof, E. Hasheminejad, Int. J. Hydrogen Energy 38 (2013) 92−99.
[20] Z. Chen, M. Waje, W. Li, Y. Yan, Angew. Chem. Int. Ed. 46 (2007) 4060−4063.
[21] C. Zhu, S. Guo, S. Dong, Chem. Eur. J. 19 (2013) 1104−1111.
[22] J. Lu, I. Do, L.T. Drzal, R.M. Worden, I. Lee, ACS Nano 2 (2008) 1825−1832.
[23] Y. Shao, S. Zhang, C. Wang, Z. Nie, J. Liu, Y. Wang, Y. Lin, J. Power Sources 195 (2010) 4600−4605.
[24] C. Xu, X. Wang, J. Zhu, J. Phys. Chem. C 112 (2008) 19841−19845.
[25] Y. Xin, J. Liu, Y. Zhou, W. Liu, J. Gao, Y. Xie, Y. Yin, Z. Zou, J. Power Sources 196 (2011) 1012−1018.
[26] X. Wang, D. Liu, S. Song, H. Zhang, J. Am. Chem. Soc. 135 (2013) 15864−15872.
[27] C. Tan, X. Huang, H. Zhang, Mater. Today 16 (2013) 29−36.
[28] Y. Lu, Y. Jiang, H. Wu, W. Chen, J. Phys. Chem. C 117 (2013) 2926−2938.
[29] W.S. Hummers, R.E. Offeman, J. Am. Chem. Soc. 80 (1958), 1339−1339.
[30] S.W. Kang, Y.W. Lee, Y. Park, B.-S. Choi, J.W. Hong, K.-H. Park, S.W. Han, ACS Nano 7 (2013) 7945−7955.
[31] W. Qian, R. Hao, J. Zhou, M. Eastman, B.A. Manhat, Q. Sun, A.M. Goforth, J. Jiao, Carbon 52 (2013) 595−604.
[32] X.W. Lou, L.A. Archer, Z. Yang, Adv. Mater. 20 (2008) 3987−4019.
[33] L. Dong, R.R.S. Gari, Z. Li, M.M. Craig, S. Hou, Carbon 48 (2010) 781−787.
[34] B. Liu, H.Y. Li, L. Die, X.H. Zhang, Z. Fan, J.H. Chen, J. Power Sources 186 (2009) 62−66.
[35] J. Datta, A. Dutta, M. Biswas, Electrochem. Commun. 20 (2012) 56−59.
[36] M. Simoes, S. Baranton, C. Coutanceau, Appl. Catal. B 110 (2011) 40−49.
[37] S. Sharma, A. Ganguly, P. Papakonstantinou, X. Miao, M. Li, J.L. Hutchison, M. Delichatsios, S. Ukleja, J. Phys. Chem. C 114 (2010) 19459−19466.
[38] L. Gao, W. Yue, S. Tao, L. Fan, Langmuir 29 (2012) 957−964.
[39] M.S. Arif Sher Shah, K. Zhang, A.R. Park, K.S. Kim, N.-G. Park, J.H. Park, P.J. Yoo, Nanoscale 5 (2013) 5093−5101.
[40] N.I. Kovtyukhova, P.J. Ollivier, B.R. Martin, T.E. Mallouk, S.A. Chizhik, E.V. Buzaneva, A.D. Gorchinskiy, Chem. Mater. 11 (1999) 771−778.
[41] W. Yue, Z. Lin, S. Jiang, X. Yang, J. Mater. Chem. 22 (2012) 16318−16323.
[42] S. Stankovich, D.A. Dikin, R.D. Piner, K.A. Kohlhaas, A. Kleinhammes, Y. Jia, Y. Wu, S.T. Nguyen, R.S. Ruoff, Carbon 45 (2007) 1558−1565.
[43] A.C. Ferrari, J.C. Meyer, V. Scardaci, C. Casiraghi, M. Lazzeri, F. Mauri, S. Piscanec, D. Jiang, K.S. Novoselov, S. Roth, A.K. Geim, Phys. Rev. Lett. 97 (2006) 187401.
[44] J.-D. Qiu, G.-C. Wang, R.-P. Liang, X.-H. Xia, H.-W. Yu, J. Phys. Chem. C 115 (2011) 15639−15645.
[45] Y. Liu, Y. Huang, Y. Xie, Z. Yang, H. Huang, Q. Zhou, Chem. Eng. J. 197 (2012) 80−87.
[46] L. An, L. Zeng, T.S. Zhao, Int. J. Hydrogen Energy 38 (2013) 10602−10606.
[47] L. An, T.S. Zhao, S.Y. Shen, Q.X. Wu, R. Chen, Int. J. Hydrogen Energy 35 (2010) 4329−4335.
[48] M.M. Dimos, G.J. Blanchard, J. Phys. Chem. C 114 (2010) 6019−6026.